

PAPER • OPEN ACCESS

Soft buckling achieves consistent large-amplitude deformation for pulse jetting underwater robots

To cite this article: Alexander O'Loughlin et al 2025 Bioinspir. Biomim. 20 056008

View the article online for updates and enhancements.

You may also like

- Photonic-digital hybrid artificial intelligence hardware architectures: at the interface of the real and virtual worlds Lília M S Dias, Dinis O Abranches, Ana R Bastos et al.
- Global evidence that cold rocky landforms support icy springs in warming mountains
 Stefano Brighenti, Constance I Millar, Scott Hotaling et al.
- ICRH modelling of DTT in full power and reduced-field plasma scenarios using full wave codes
 A Cardinali, C Castaldo, F Napoli et al.

Bioinspiration & Biomimetics



OPEN ACCESS

RECEIVED

1 May 2025

REVISED

22 July 2025

ACCEPTED FOR PUBLICATION 14 August 2025

14 Mugust 20.

PUBLISHED

4 September 2025

Original Content from this work may be used under the terms of the Creative Commons Attribution 4.0 licence.

Any further distribution of this work must maintain attribution to the author(s) and the title of the work, journal citation and DOI.



PAPER

Soft buckling achieves consistent large-amplitude deformation for pulse jetting underwater robots

Alexander O'Loughlin^{1,*}, Samuel Simmons¹, Melike Kurt¹ and Blair Thornton^{1,2}

- Maritime Engineering Group, Faculty of Engineering and Physical Sciences, University of Southampton, Southampton, United Kingdom
- Institute of Industrial Science, The University of Tokyo, Tokyo, Japan
- * Author to whom any correspondence should be addressed.

E-mail: ajo1g20@soton.ac.uk

Keywords: pulse jetting, low frequency, soft robotics, bioinspired swimming, lateral buckling, jellyfish Supplementary material for this article is available online

Abstract

Jellyfish achieve efficient pulse jetting through large-amplitude, low-frequency deformations of a soft bell. This is made possible through large localised deformations at the bell margin. This paper develops a novel soft-robotic underwater pulse jetting method that harnesses the buckling of flexible tubes to generate thrust. Soft material instability is controlled through variation of internal water pressure in the tubes, where we demonstrate repeatable large-amplitude deformations with bell flexion angles of $29 \pm 1.5^{\circ}$ over a frequency range of 0.2-1.1 Hz. The actuator is used to propel a soft robotic platform through water, achieving instantaneous velocities of up to 5 cm s⁻¹ with no noticeable degradation in performance over 1000 pressure cycles.

1. Introduction

Underwater robots are routinely used to study marine environments and ecology in challenging and delicate environments [1, 2]. Although such surveys are typically carried out by conventional, rigid submersibles actuated by propellers and control surfaces, soft robotic systems have the potential to increase propulsive efficiencies and reduce the risk of damage to both the robots and the fragile ecosystems they operate in. However, bioinspired designs do not yet achieve the efficiency of their natural counterparts or the versatility and wide operating range of propellers. These gaps need to be reduced to take greater advantage of soft actuators in underwater robot designs.

The high rotation rates and tip speeds of propellers create unsteady wakes. In shallow water (i.e. low hydrostatic pressure), low pressure zones around the rotating blades can cause cavitation and multi-phase flow, generating noise at low frequency ranges (10–1000 Hz) that are known to affect marine wildlife [3, 4], and interfere with acoustic communication [5]. Bioinspired propulsors typically operate at frequencies closer to those of marine life, offering a potential alternative for underwater propulsion with reduced environmental impact.

Pulse jetting is a mechanism used by natural swimmers that alternately contract and expand a flexible cavity (bell) to accelerate the fluid mass and generate thrust. Pulse jetting shows one of the highest energy efficiencies among natural swimming techniques [6]. Whilst pure pulse jetting is suitable for creating rapid accelerations, jellyfish achieve efficient continuous propulsion with the addition of a paddling action into the cycle [7, 8]. The paddling action relies on a highly flexible bell margin, which undergoes large deformations along a short section of the cavity wall, maximising the circulation of vortices formed at the margin [9]. The stopping vortex from the expansion phase and the starting vortex from the following contraction phase pair up and convect downstream. This vortex pair features a central jet with high velocity in the direction opposite to the jellyfish motion [10]. This vortex interaction helps to reduce drag during the expansion of the bell, aiding swimming efficiency and reducing the loss of kinetic energy in the wake [11].

Jellyfish anatomy allows for large deformations of a gelatinous *mesoglea* between the epidermal and endodermal layers [12]. The mesoglea has a sufficiently low stiffness to maintain the structural integrity of the cavity wall whilst allowing for large

elastic deformations. The location of maximum compressive deformation in the mesoglea has an estimated stiffness of 50 Pa, compared to a stiffness of 352 Pa for the broader bell mesoglea [13]. Reproducing the large localised deformations seen at the bell margin, whilst maintaining a controlled and repeatable flapping motion, has yet to be reproduced by a bioinspired robot. This can be attributed to the difficulty in manufacturing and controllably manipulating extremely flexible materials.

Several underwater soft robot actuation techniques have demonstrated pulse-jetting. Villanueva [14, 15] used shape memory alloys and linear actuation of mechanical arms, both of which relied on movement of stiff materials, to manipulate a soft body. Bujard [16] demonstrated resonance of a soft bell to achieve efficiency similar to nature's most efficient swimmers, but the mechanism relied on rigid mechanical arms to deform the soft material. The resonant frequencies achieved were significantly higher than those of natural swimmers. Another soft robotic platform, PoseiDRONE [17] controlled an entirely soft bell using adhered cables to contract the bell. The approach achieved large volume changes, but the deformation pattern was uncontrolled and governed by the location of cable attachment points on the thin walls of the bell. The system relied on the elastic potential of the material to passively restore the bell to its natural shape, which limited the operable frequencies since the fluid ingestion rate could not be controlled [18].

Control of both frequency, f, and amplitude, A, to optimise soft robot swimmer efficiency is non-trivial. The Strouhal number relates these variables to swimmer speed, U and is defined as,

$$St = \frac{2fA}{U}. (1)$$

Most flying and swimming animals operate within $0.15 \le St \le 0.8$ [19, 20]. Such Strouhal numbers have been achieved by soft robots, but required a different ratio of frequency to amplitude compared to the examples in nature. Typical swimmers and flyers operate with a flexion angle of $\sim 27^{\circ}$ [21], with bats, some fish, and molluscs exceeding 40° whilst operating at low actuation frequencies due to the high inertial loads imposed by water. Typical pulse jetting swimmers operate at around 0.6 Hz [6], an order of magnitude below existing efficient pulse jetting robots [16]. The desire to unlock biological efficiency and manoeuvrability drives investigation into generating large amplitudes at low frequencies.

This study leverages material instabilities to access large amplitude deformations at low frequencies. Taking inspiration from jellyfish anatomy, thinwalled flexible tubes are used to maintain their structure (higher stiffness), and buckle (lower stiffness) through pressurisation or depressurisation of an internal incompressible fluid. Pressurisation of inflatable tubes to control the stiffness of flapping foils has been investigated, where Micklem et al [22] demonstrated that a foil could be tuned to a range of natural frequencies by adjusting the second moment of area of the foil using inflatable tubes. To achieve the large angle deformations needed for the bell margin of a pulse jetting robot, a significantly higher and more localised change in second moment of area is required. Our hypothesis is that this large change in the second moment of area can be efficiently achieved through material instability, specifically the elastic buckling of flexible tubes, producing a controllable 1 degree of freedom flexible joint. Elastic buckling could allow for a snap-through response, similar to those experienced by bistable systems, if internal pressure is rapidly changed, but controlled pressure change also has the ability to provide continuously stable actuation, allowing for variable frequencies and amplitudes.

Numerous existing methods are capable of providing soft actuation, bypassing the need for mechanical joints. Pneumatic and hydraulic muscles operate through a principle where the change in a tube (bladder) cross-section drives the shape change. The bladder is wrapped in a non-extensible mesh sleeve, which restricts the system from expanding radially and allows for axial contractions only. While such pneumatic and hydraulic systems can mimic muscle contraction or extension through simple expansions of an extensible tube, much larger, localised deformations become possible through buckling. Achieving larger amplitudes with pneumatic systems, similar to buckling, requires a longer actuator and a larger volume of fluid for pressurisation [23]. Pneumatic muscles exhibit non-linear behaviour under large strain, which is also to be expected from a buckling system. As a result of energy losses from material strain, both methods exhibit hysteresis between expansion and contraction phases [24]. Efficiency of pneumatic muscles vary, but are typically within the range of 20%–50% [25, 26].

Dielectric elastomers have also been used in bioinspired robots [27], enabling them to provide deflections through independently controlled actuators on either side of a soft body. When a voltage is put across the elastomer, it undergoes expansion, and a voltage difference on either side of the soft body leads to an angular deflection. Using very thin bodies, large localised deformations can be achieved [28]. Whilst dielectric elastomers have potential for high efficiencies (max. 90%) [29], practical applications struggle to reach 40% [30-32], with increasing frequencies (required to provide large forces) a key contributor to reductions in efficiency. Dielectric materials also have risks when operating in salt water, with highstrain dielectric materials at high risk of hydrolytic degradation and subsequent reductions in strength and elasticity [33].

Table 1. Young's moduli of natural swimmers [40, 41], naturally buckling components [42], and synthetic materials [43, 44].

Material	Young's modulus [Pa]	
Jellyfish mesoglea	3.5×10^{2}	
Squid mantle	1.0×10^{6}	
Earthworm cuticle	1.3×10^{6}	
Silicone rubber	$5.2 \times 10^5 - 6.2 \times 10^7$	
Flexible PVC	$5.5 \times 10^6 - 3.2 \times 10^9$	

Tensegrity structures show promise for bioinspired designs [34], with a number of designs for bioinspired propulsors appearing in literature, but few having made it beyond theory or preliminary testing [35, 36]. The high complexity and relatively limited localised deflection capabilities have diverted research away from propulsors, instead, targeting high fidelity operations, including mechanical arms and systems for exploration in highly confined spaces [37, 38].

In many scenarios, buckling is considered a form of catastrophic plastic failure that should be avoided. However, flexible materials can buckle while remaining in the elastic regime. This technique is demonstrated in nature by earthworms, which buckle their cuticle to aid locomotion, particularly while navigating flowable substrates [39]. Table 1 shows that the Young's modulus of the most flexible silicone rubber samples is similar to the earthworm's cuticle, suggesting that cyclic buckling of silicone can be performed without experiencing plastic deformation.

Two soft buckling actuators made of silicone rubber tubes on either side of a bell cavity were used to replicate the expansion and contraction motions of a jellyfish. Flat plates constrained the fluid in the spanwise direction, making the body consistent with the two-dimensional cross-section of a jellyfish bell. Using the soft buckling platform, we achieved large deformations during pulse jetting while maintaining the structural integrity of the bell. Our experiments demonstrate that this approach yields repeatable results, consistent across a wide range of actuation frequencies, with no noticeable material degradation observed over 1000 actuation cycles. The proposed propulsion method could better replicate the efficient, low-frequency motions used by jellyfish to generate thrust, using only a small number of mechanical components with the potential to form an entirely soft bell.

2. Experiments in air

When an unbuckled soft tube acts as a cantilever, its deflection subjected to an endpoint load can be estimated from simple beam theory.

$$D = \frac{FL^3}{3EI},\tag{2}$$

where *F* is the contractive force, *L* is the length of the tube, E is the Young's modulus, and I is the second moment of area. For an inextensible tube, where pressure does not influence the second moment of area, deflection is constant for a given force, regardless of internal pressure [45]. This assumes that the internal volume of the tube is unchanged, therefore, it is only appropriate for small angle deflections. With highly flexible tubes, some variation in deflection can be expected by varying internal pressure. When buckling occurs, the second moment of area reduces at the location of the hinge formation, and the tube's deflection increases significantly. Whilst increasing pressure does not directly influence the second moment of area in pure bending, it will delay the onset of buckling. For any tube, an internal pressure, P, has a corresponding critical buckling force, $F_{\rm crit}$. For a pressure range, $P_{\rm range}$, where $P_- \leqslant P \leqslant$ P_{+} , the tube will be able to buckle and unbuckle purely by cycling between maximum and minimum pressures.

The selection of $P_{\rm range}$ is important to minimise the required energy input. Increasing pressure when unbuckled is not expected to produce any foil deflection; thus, no useful work is produced. Energy losses occur when a material experiences high deformations, thus there is expected to be a hysteresis between pressurisation and depressurisation phases. It was expected that unbuckling would require a higher pressure than the initial buckling, as some of the potential energy providing a restoring force to the tube dissipates as the material strains, thus a higher fluid pressure is required to compensate.

Before building a swimming system, there is a need to understand the buckling behaviour. To investigate the buckling hysteresis during expansion and contraction, and to explore the required internal pressure change, P_{range} , and the tube length for efficient buckling, we conducted experiments in air with buckling silicone rubber tubes.

2.1. Hysteresis from buckling

To investigate the hysteresis of buckling, a tube was set up as a cantilever with an end mass (48 g) positioned such that the unbuckled deflection brought the cantilever tip parallel to the ground, applying a force, F, perpendicular to the tube. The end mass, providing the moment for buckling, was situated 7 mm beyond L, thus the lever arm from the cantilever root, L_M , is equal to L+7. We used silicone rubber tubes with a measured Young's modulus of 1.30 MPa. The tubes had an internal diameter, d, of 8 mm and a wall thickness of 0.999 ± 0.0066 mm, preventing plastic deformation while maintaining suitably low expansion under pressure. The tubes were constructed by stretching silicone tubing over 3D-printed polylactic acid plugs, with a layer of superglue to ensure a watertight seal. The internal pressure was controlled through an inlet in one end plug.



Figure 1. (a) A tube with high internal pressure, such that $F \approx F_{\rm crit}$, and a buckle has just begun to form. This points corresponds to the upper 10% bound in figure 2. (b) Internal pressure has reduced such that the corresponding $F_{\rm crit}$ no longer exceeds F and the tube has buckled. The buckle is not yet at maximum deformation, and further reduction in P would result in greater deflection. This experiment is shown in supplementary video 1.

Four tubes with a flexible length of 32 ± 2 mm were used to conduct the hysteresis experiments in air via pressurisation and depressurisation of the tubes. Each tube experienced two cycles, with a cycle spanning from $P_{-} = 0$ kPa, to $P_{+} = 60$ kPa, a pressure that is sufficient to fully unbuckle the tube. The amplitude, h, was measured as the vertical displacement of the mass attachment point. Figure 1 shows the setup used, as the tube switches from an unbuckled state to an intermediate buckling state. In figure 1(a), the internal pressure is sufficient to maintain a near fully unbuckled state, but we can see a hinge starting to form. As the internal tube pressure is decreased, the tube buckles further. Figure 1(b) shows an intermediate buckling state where the tube has buckled, but the internal pressure within the tube can still partly support the end load, and displacement is not yet at a maximum. Figure 2 presents the change in amplitude against the applied pressure. For efficient buckling operation, it is recommended to avoid the minimum and maximum amplitude, as the rate of amplitude change against pressure change is very low in these regions. Buckling efficiency has been calculated excluding the pressure required to produce the upper and lower 10% amplitude changes, shown by the dashed lines in figure 2.

2.2. Buckling efficiency

The indirect use of buckling forces to control the state of a soft bell requires design optimisation. Efficiency, η , is defined as the ratio of potential energy to elevate the end mass, m, through an amplitude change, Δh , to the energy supplied to increase the pressure in the tubes by $P_{\rm range}$. Here, η can be expressed as,

$$\eta = \frac{mg\Delta h}{LSP_{\text{range}}} \tag{3}$$

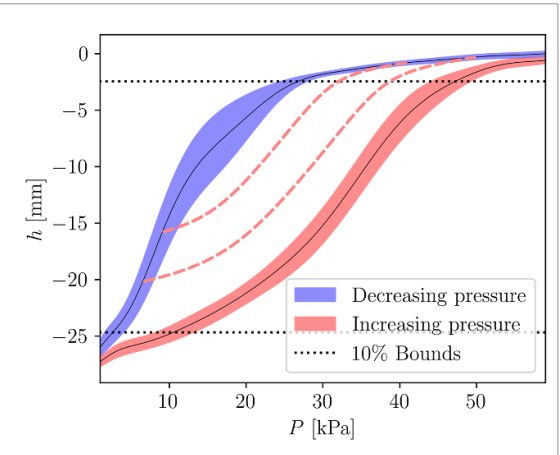


Figure 2. Amplitude against internal pressure for a buckling tube with a 48 g end mass. A clear hysteresis is visible between the inflation and deflation curves (error bands are calculated using the standard error of the mean, SE = $\frac{\sigma}{\sqrt{n}}$). Buckling efficiencies have been calculated for the region enclosed by the 10% bounds. Red dashed lines represent potential increasing pressure curves if P_- is controlled, thus reducing the buckling amplitude and the required input energy.

where g is acceleration due to gravity and S is the cross-sectional area of the tube.

Increasing the load acting on the pressurised cantilever tube allows a larger produced force, thus, a larger thrust to be exerted when the tube buckles. However, this also results in a larger P_{range} necessary to generate the same amplitude. Similarly, an increase in tube length enables a larger range of motion between buckled and unbuckled states. The influence of the applied mass and tube length on buckling efficiency was investigated experimentally. Using the same setup (figure 1), tubes with lengths 30 mm, 40 mm, and 50 mm, each experienced buckling forces of 0.38 N, 0.58 N, and 0.79 N. Additionally, the tube parameters used later in free swimming experiments (16 mm and 1.08 N) have been added. The change in buckling efficiency against the variations in tube length and the applied force is presented in figure 3, with the x-axis set such that η has a linear response to the changes in length and force. This linearisation produces a plot where $\eta \propto L_M^{-1} L^{-1} F^{-0.5}$.

Figure 3 shows that there is an inverse correlation between both tube length and applied moment, and efficiency, with changes in length having a greater influence $(\eta \propto 1/(L_M L) \text{ vs. } \eta \propto 1/\sqrt{F})$. The trendline intersects the origin, which confirms that as $\lim_{L\to\infty}$, $\eta(L)=0$, and $\lim_{L_M F\to\infty}$, $\eta(L_M F)=0$. This suggests that the tube length and contractive moment should be kept as low as possible. The linear trend is expected to break down at some point before $\eta=100\%$. This can be attributed to the existence of a minimum required moment and tube length for buckling to occur unrestrained. The L term arises in a direct link to equation (3), whereby $\eta \propto L^{-1}$. Supplied power is proportional to the volume of the tube and therefore the tube length. Outside of the buckling

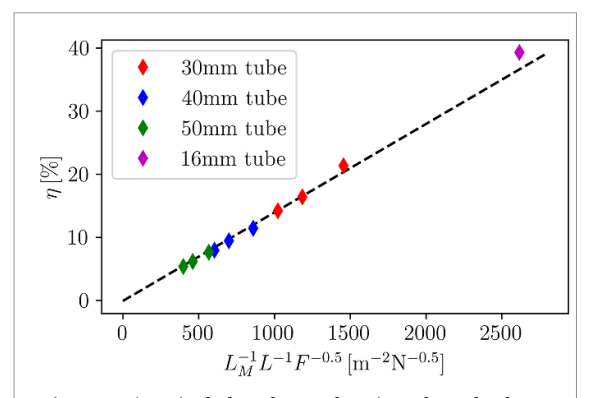


Figure 3. Linearised plot of η as a function of L and F from the initial experiments in air, with a linear trendline intersecting the origin plotted. The average error between the experimental data and linear trendline is 3.18%. The tubes used later in free swimming experiments have been added in purple, and show a 7.3% improvement over the predicted trend.

region no useful work is produced, thus, all supplied energy is wasted.

3. Materials and methods for a free swimming platform

3.1. Soft robot design and actuation

A bioinspired robotic platform actuated via buckling flexible tubes has been developed and tested to investigate the repeatability and usability of soft buckling as a method for marine pulse jetting. The flexible tubes characterised through the experiments in air have been used with the tube length limited to twice the tube internal diameter, 16 mm, without hindering the buckling motion (It is expected that this length can be further reduced whilst maintaining the target flexion angles, increasing efficiency towards 60% without compromising the buckling motion). The free-swimming experiments were carried out using the actuator in figure 4(a), connected to the robotic platform shown in figure 4(c). A full schematic of the experimental setup is shown in figure 4(b). The robotic platform is immersed in a water tank $(4.5 \text{ m} \times 2.5 \text{ m} \times 1.2 \text{ m})$, and the pressure change prescribed through the actuator drove the paddling motion through repeated buckling and unbuckling of the flexible tubes.

The robotic platform shown in figure 4(c) had two tubes on each side of the bell to ensure buckling in the desired two-dimensional plane. These tubes were angled 60° apart at the root, with the permanent deflection determined by equation (2) bringing the tube ends to near parallel when unbuckled. A solid paddle was attached to the end of the tubes on each side, with a floating hinge at the location of buckling. This hinge allowed for unrestricted rotation between the robot body and paddles, preventing the

rigid structure from impeding the buckling motion and limiting the fluid outflow through the bell edges. Whilst this body was not entirely soft, the solid paddles were connected to the swimmer's body via the flexible buckling tubes only. Elastic bands were connected between the paddles on either side, providing the contractive force necessary to induce buckling. Clear acrylic panels were fitted to the front and back of the robot to restrict the tip flow around the solid paddles. Within the main body of the robot, the inlet plugs of the buckling tubes were joined to a single flexible feeder hose via a four-way junction, contained in a hydrodynamic housing. The four-way junction ensured that the pressure within each tube was equal at all times and allowed pressure to be controlled by an external pump. Hooks were installed at both ends of the swimmer, allowing artificial buoyancy control via suspended masses on either side, as shown in figure 4(b).

Internal pressure in the buckling tubes was varied using a 20 ml syringe connected to the feeder hose, using water as the working fluid. Compression and expansion of the syringe was controlled by a variable speed actuator, composed of a DC motor rotating a cam and driving a crank attached to the syringe plunger. The system, when disconnected from the actuator, passively returns to ambient pressure. Here, only the motor requires (non-negligible) energy input during pressurisation above ambient pressures or to create a partial vacuum. For the rest of the pressure cycle, the motor controls the pressure reduction in order to produce a consistent sinusoidal pressure. A pressure transducer was attached to the feeder hose at the syringe, which output a signal to an oscilloscope to determine internal pressure and frequency. Figure 5 shows the measured pressure throughout the cam cycle, along with the corresponding position of the cam during the expansion phase. The measurements indicate a near sinusoidal pressure cycle with minor discrepancies due to the crank arm angle and deformations of the plunger. Due to the low frequency actuation used for these experiments, there is minimal delay between pressurisation and the structural response and imposed kinematics. Input energy is required for the partial vacuum formation and pressurisation, from $0.3 \leqslant t/T \leqslant 0.5$, and $0.7 \leqslant t/T \leqslant$ 1.0, respectively. Throughout the experiments, P_{range} varies slightly across the frequency range, resulting in up to 10% deviations around the pressure cycle maxima at higher frequencies. This is likely a result of friction in the feeder tube, which caused an increase in pressure on the actuator when operating under higher loads. Across the frequency range, the average P_{range} was measured to be 60 kPa. Figure 6 shows a series of images taken from the platform immersed in

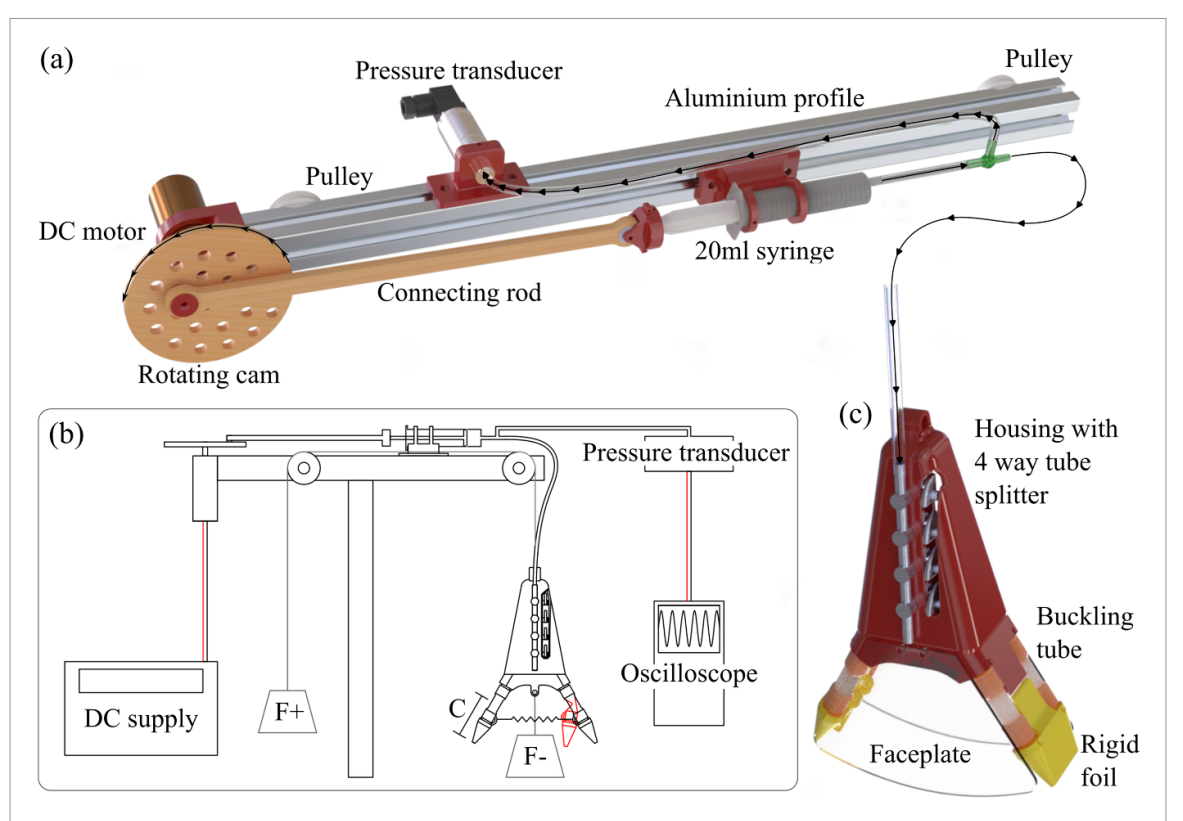


Figure 4. (a) 3D design of the actuator used to control internal pressure within the buckling tubes and record pressure data during experiments. A brushed DC motor controlled by a variable voltage supply drove a cam, producing linear motion to drive the syringe plunger. (b) Schematic of the experimental setup. (c) Design of the robotic platform used for free-swimming experiments.

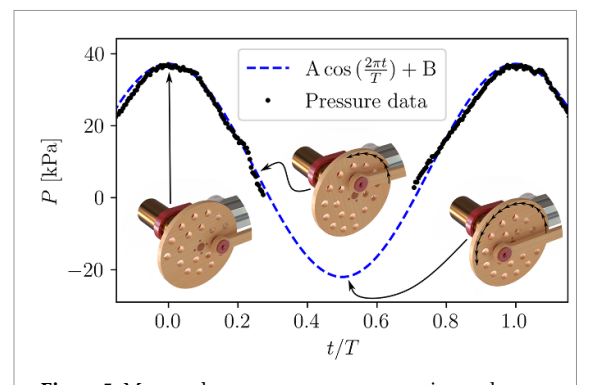


Figure 5. Measured pressures across an actuation cycle, taken from a run at 0.4 Hz. Only positive pressure data is available, and a cosine wave has been fitted to predict the negative pressures within the cycle (A=29.6, B=7.6). A total pressure change of \pm 59.2 kPa per half rotation of the cam was generated.

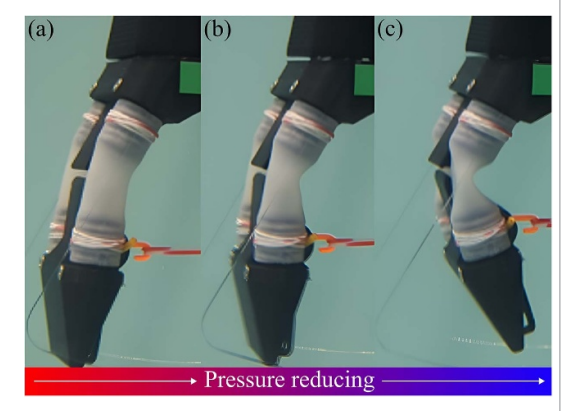


Figure 6. (a) $P = P_+$, all tubes are unbuckled and the bell cavity is at maximum volume. (b) $P_- \le P \le P_+$, the tubes have begun to buckle, but the amplitude is still low. (c) $P = P_-$, the bell amplitude is at a maximum, and a significant buckle is showing in the flexible tubes.

3.2. Free swimming experiments

The primary aim of free swimming experiments was to determine the consistency and repeatability of buckling over a range of biological actuation frequencies whilst attaining a buckling amplitude similar to the flexion angles achieved by natural swimmers.

For the free-swimming experiments, buoyancy of the robot was tuned by adjusting F_+ and F_- using masses attached to a fishing line and pulley system. A similar pulley system was used to draw the feeder hose out of the water, reducing the impact of hose

bending on the swimmer's motion. Whilst in motion, hydrodynamic drag, $F_{\rm drag}$, and dynamic frictional drag, $F_{\rm friction}$, both contribute to resist the swimmer's motion. Due to the low speed of the underwater body, we expected the system friction to be much larger than the hydrodynamic drag, $F_{\rm friction} >> F_{\rm drag}$. The dynamic frictional drag varies with the first power of velocity, $F_{\rm friction} \propto V$. For constant velocity free-swimming, we can assume thrust to vary accordingly to overcome this drag, thus, $F_{\rm thrust} \propto V$.

To prevent static frictional forces from adding a third drag component, F_+ was increased to make the robot slightly positively buoyant, resulting in a permanent positive velocity. The swimming speed, V, and the pulse jetting force, $F_{\rm thrust}$, were then calculated relative to the non-swimming, positively buoyant robot. The non-swimming velocity was measured for both the unbuckled and buckled profiles, and the average was taken as the reference velocity (V=0).

During swimming, an increase in frequency was expected to result in an increase in thrust through two separate contributions. Higher frequencies increase the number of force-generating pulses per second and the acceleration of the expelled fluid mass within each cycle. Based on these simplified assumptions, it was approximated that the pulse jetting force correlates with the second power of pulsing frequency, $F \propto f^2$, and consequently, $V \propto f^2$, assuming the drag force is dominated by frictional components.

Nine frequencies between 0.2 Hz $\leq f \leq$ 1.1 Hz were investigated, covering the range of frequencies of most natural swimmers. For each frequency, as well as the static swimmer in both the buckled and unbuckled state, the swimmer's vertical velocity, V, was calculated from the average time taken to translate between two points. During experiments, the order of the nine actuation frequencies was randomised and each frequency was tested 3 times (except the top two which were only performed once to prevent the motor from getting damaged). All experiments were recorded using a camera at 30 FPS. With the highest swimming frequency of 1.1 Hz, this resulted in a minimum of 27 frames spanning an actuation cycle, allowing amplitude measurement within a single cycle.

3.3. Comparison to computational fluid dynamics (CFDs)

CFDs simulations over a two-dimensional domain have been performed to compare the vortex generation of the free swimming platform to that of biological jellyfish, and to predict swimming speed in a frictionless environment. The WaterLily framework solves the incompressible Navier-Stokes equations and performs turbulence modelling using implicit large eddy simulations (LESs) [46]. A domain size of 49 152 cells was used and the simulation was insensitive to further spatial refinement (2% change when increased to 196 608 cells). Due to the body shape of the free-swimming platform, it was not possible to directly validate the generated forces with that of biological jellyfish or other CFD from literature. There is strong correlation in the location of force peaks and troughs with the CFD of natural jellyfish motions [6], but the magnitude of energy recapture during the expansion phase is noticeably higher in literature, likely a result of the more complex motions explored.

Simulations were run with constant inflow velocity, thus accelerations of the body are not

captured. The predicted swimming velocity of the body at different actuation frequencies has been determined as when the time-averaged thrust and drag on the body over 2 complete actuation cycles are equal. Reynolds number, Re = VL/ν (where ν is the kinematic viscosity of the working fluid), and St have been matched to free-swimming experiments. Swimming velocity from simulations is expected to be proportional to the actuation frequency, in contrast to the free-swimming experiments. $F_{\rm drag} \propto V^2$ and $F_{\rm thrust} \propto f^2$. For free swimming, $V \propto fA$ [47]. Thus, at constant motion amplitude, it can be stated that $V \propto f$.

3.4. Free swimming results and discussion

Figure 7(a) presents the time-averaged swimming speed, V, across different actuation frequencies, f. A curve fit of $V \propto f^{1.8}$ was found to be a better representation of the experimental data within the tested frequency range, compared to the previously predicted trend, $V \propto f^2$. This deviation is due to the assumption that $F_{\text{friction}} \propto V$. Whilst V is sufficiently small, this assumption should hold true. However, the instantaneous velocity, V', experiences peaks and troughs within each pulse-jetting cycle, as shown in figure 7(c). At the lower frequencies, f = 0.4 and 0.8 Hz, the maximum instantaneous velocity is 3.4 times the time-averaged velocity, $max(V')/V \approx 3.4$. At the highest frequency considered, f = 1.1 Hz, this ratio reduces to $max(V')/V \approx 2.6$. This can be attributed to the drag component becoming more influential at the higher velocities, reducing the maximum instantaneous velocity, and producing the deviation from the predicted $V \propto f^2$ trend. Speeds predicted by LES are larger than those measured from the freeswimming platform (\sim 5 times higher at 1.1 Hz), due to the simulations being a frictionless system. Simulations follow a linear trend (with some oscillation) as predicted.

The instantaneous amplitude, A', for four runs has been compared and plotted in figure 7(b), with data taken at frequencies of 0.2, 0.4, 0.8, and 1.1 Hz. Across this frequency range, the waveform remains largely unchanged, showing that the buckling mechanism has high repeatability and exhibits large and near-constant amplitude deformation over the entire investigated frequency range. Table 2 shows the average peak amplitude, A, and variability (standard error) across experiment batches, with no significant change over 1000 cycles. Buckling amplitude is a direct response to the material properties. Thus, no change in amplitude confirms that there was negligible or no degradation in the system.

This consistency across the frequency range confirms that buckling is a viable means of actuation for bioinspired robots aiming to actuate with similar parameters to natural swimmers. The usual flexion angle for natural swimmers of 27° was exceeded, with an average buckling amplitude of 29.3° for

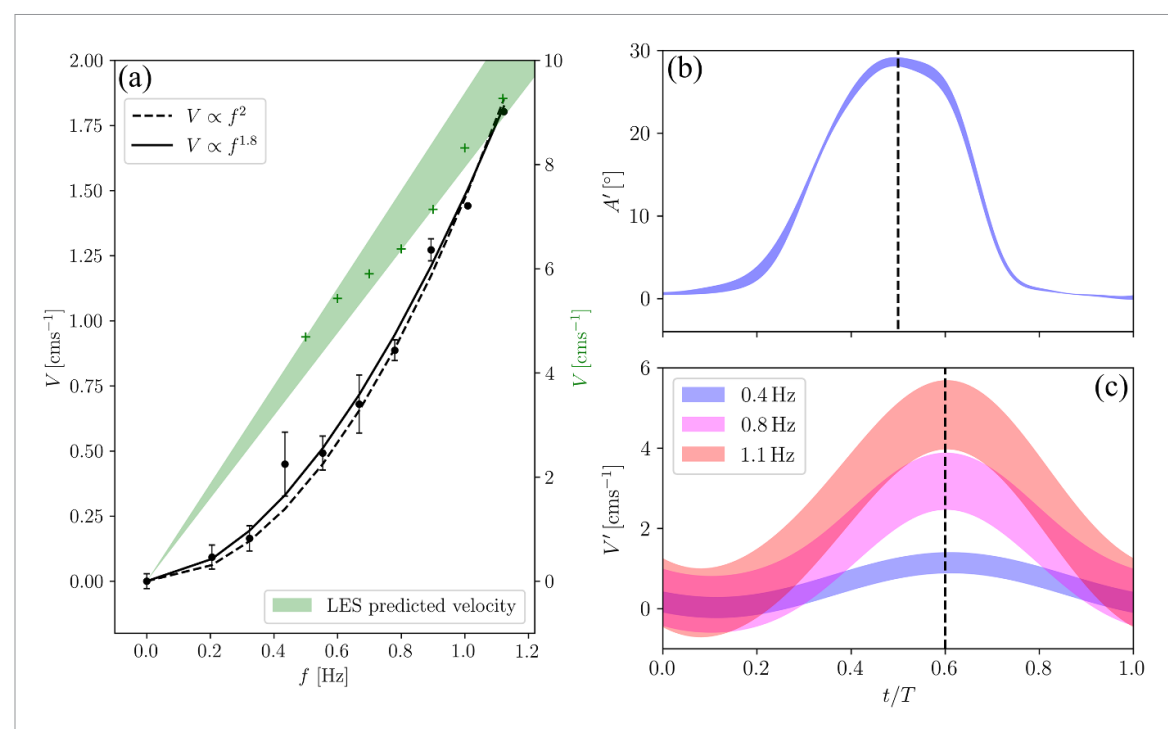


Figure 7. (a) Relative velocity against actuation frequency. Error bars are calculated as the standard error of the mean across three sets of experiments at each frequency. The highest two frequencies only have data from one experimental batch. A video comparison of swimming speed against actuation frequency is provided in supplementary video 2. Swimming speeds from LES are plotted on a secondary axis. The time-averaged Re for free-swimming experiments peaked at 6100 at the highest frequencies, with comparable LES at 17 500. (b) Cycle-averaged amplitude across the acquired time-series at four different frequencies, 0.2 Hz, 0.4 Hz, 0.8 Hz, and 1.1 Hz. The shaded region represents the standard error of the mean across the cases. The peak amplitude is centred, occurring when t/T = 0.5 (c) Instantaneous velocity of the body across a cycle, fitted using a Gaussian process with a $\pm 1\sigma$ confidence band. Much of this uncertainty comes from the differentiation of positional data from the camera images, where the low swimmer speed and high recording frequency produces oscillations around the mean V'. The maximum velocities occur with a lag of t/T = 0.107 when compared to the amplitude, a response to body inertia and asymmetrical forces produced across the actuation cycle. At 1.1 Hz a maximum Re of 13 700 is experienced.

experiments at biological frequencies of $0.6 \text{ Hz} \pm 0.3$. Crucially, this amplitude was possible using only a 16 mm length of tubing (L=2d), confirming that buckling can be used to replicate the localised high deformations seen at the bell margin of many efficient pulse-jetters.

Despite using symmetrical expansion and contraction, atypical for pulse jetters, the vortex generation from LES has captured the predicted trends from literature. These vortices are shown across a complete cycle in figure 8.

Locomotive efficiency can be measured using cost of transport (CoT), defined as:

$$CoT = \frac{P}{mU} \tag{4}$$

where P is the power supplied to the system (often taken as metabolic power for natural swimmers due to the difficulty in isolating the propulsive power), m is the mass of the system, and U is the velocity of the body. The produced CoT (with units of $Jkg^{-1}m^{-1}$) thus measures the energy required to move a mass over a distance. CoT for a range of biological swimmers, as well as a number of vehicles and robots, is shown in figure 9. The CoT of the free-swimming experiments is in line with that of existing robots and vehicles, and the increased velocities predicted from

Table 2. Average peak amplitude across experiment batches, where an experiment batch spans one experimental run at each frequency between 0.30 and 0.90 Hz, and the variability (standard error) shown for each batch.

Experiments	Cycles	A [°]
1	100 – 399	29.2 ± 0.7
2	400 - 699	29.2 ± 0.5
3	700 - 1000	29.6 ± 0.4

CFD for a frictionless system brings the CoT ahead of most existing robots.

To increase system efficiency, the peak pressure reached at the end of the unbuckling phase could be reduced, as there is no noticeable change in amplitude when phase $= 0 \rightarrow 0.15$ and $0.85 \rightarrow 1$. Once the tube is fully unbuckled, supplied energy no longer contributes to thrust generation. During the buckling phase, there is no sustained flat spot at P_- , shown in figure 7(b). An approximately sinusoidal pattern is maintained at maximum amplitude, matching the sinusoidal pressure input from the rotating cam in figure 4(a). Further reductions to P_- are likely to further increase the buckled amplitude but would also impose greater stresses on the soft material in the buckling zone.

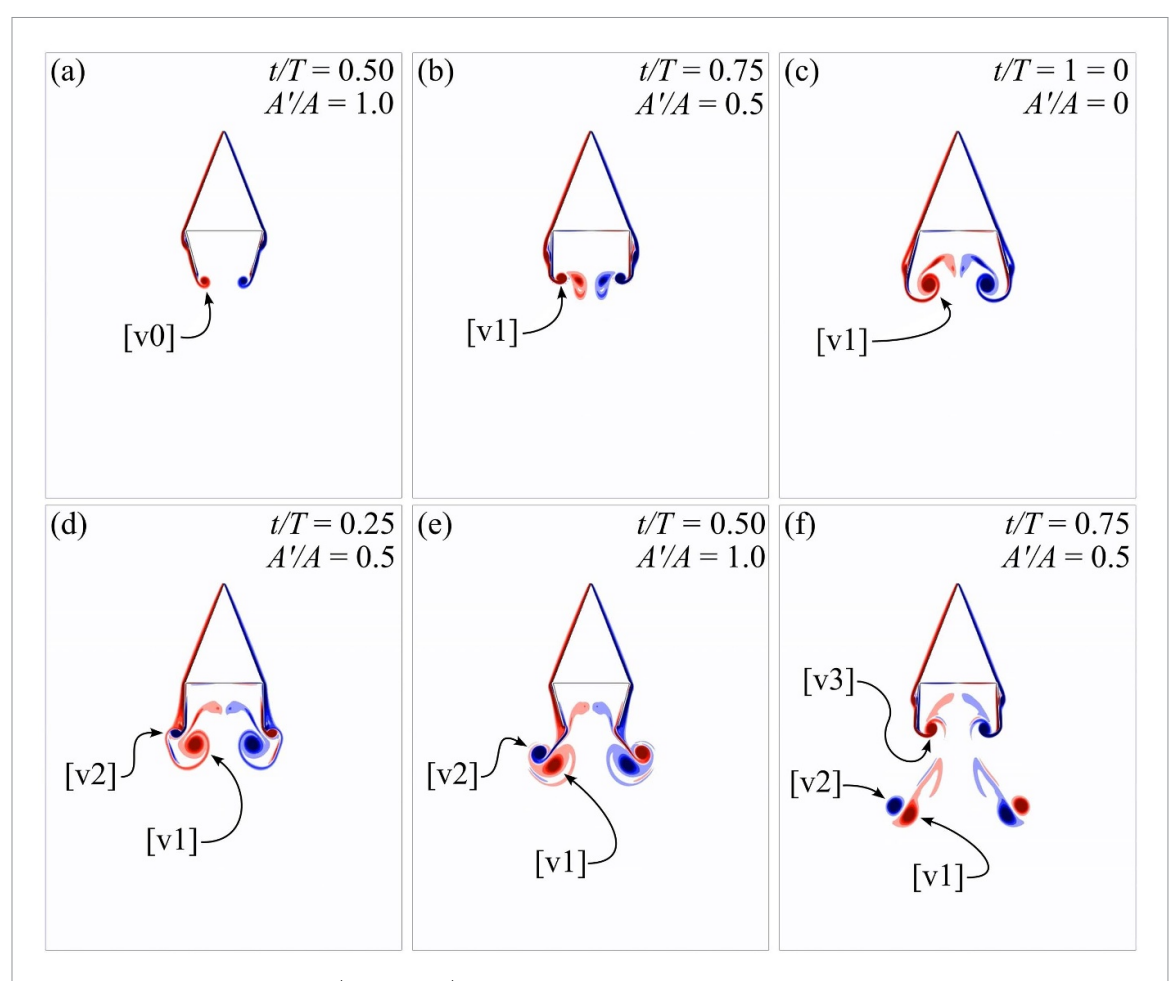


Figure 8. Vortex generation from t/T=0.5 to t/T=0.75 on the following cycle. (a) The body is initially stationary in a flow. Amplitude is at a maximum. The vortex v0 is formed from flow over a bluff body. (b) v1 is the beginning of the stopping vortex, as the bell expands and fluid is drawn into the bell. (c) v1 is held close to the body. External flow would typically carry vortices away from the body, but the drawing of fluid back into the body has held the stopping vortex at the bell orifice throughout the expansion. (d) The contraction phase takes place, and the starting vortex, v2, is formed. The starting vortex interacts with the stopping vortex, v1, enhancing circulation of both vortices. (e) The end of the contraction phase, and the vortex pairing of v1 and v2 translate downstream. The opposing directions of these vortices produces the central jet between them, where fluid velocity is at a maximum. (f) The vortex pairing stays together in the wake as momentum dissipates into the ambient fluid. A new stopping vortex, v3, is produced as the bell re-expands, and the cycle repeats.

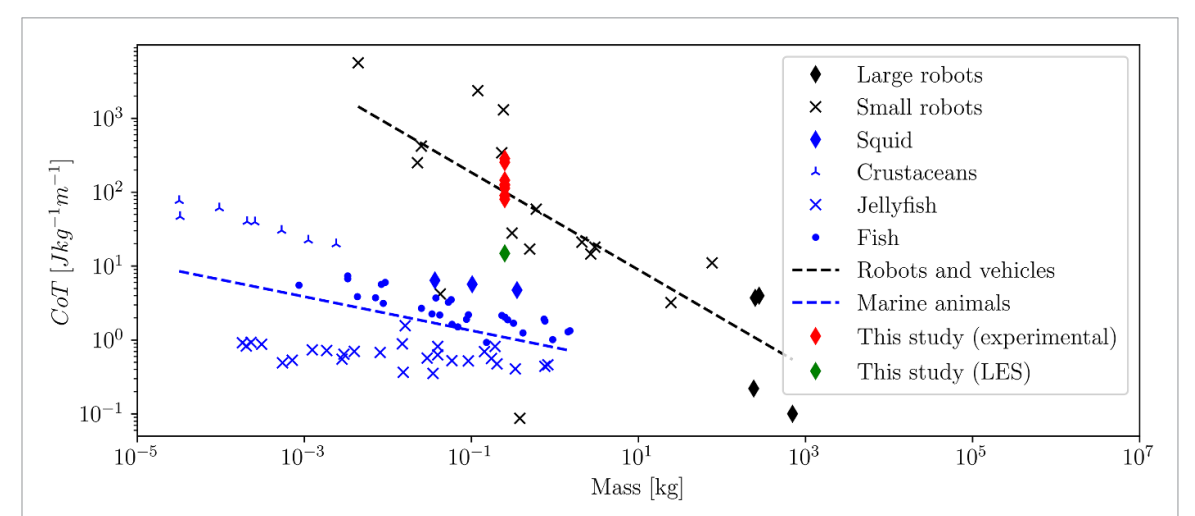


Figure 9. *CoT* against mass for various robots, vehicles, and natural swimmers, for which each has a separate trend line. Natural swimmer *CoT* is plotted from [6], and small robot *CoT* is taken from [48]. Commercial vehicle data is obtained from [49–52].

When the tubes buckle, the elastic bands were responsible for the contraction of the bell. Across the frequency range tested, this contraction was consistent, which showed the repeatability of the buckling action. However, at higher frequencies, we expect a lag between the pressure and amplitude change, resulting from increased drag and resistance from added mass on the paddles. This lag can produce a higher thrust force, as the lower internal tube pressure will provide less of an unbuckling force. To maintain operation within the biological frequency range, this could also be achieved by increasing the size of the paddle, thus increasing the resistance to contraction at lower paddle speeds. However, operating with too high a lag could result in lower amplitudes and would need careful consideration of material and spring properties. The pressure cycle can also be manipulated to be asymmetric, with a faster depressurisation (bell contraction) followed by a steady state period at P_{-} to achieve maximum amplitude and a glide, followed by a slower pressurisation (bell expansion) to reduce the drag force from fluid ingestion. This is a recommended area for future work, as it is expected to provide improvements in locomotive efficiency without a substantial increase in required power.

It is expected that independent actuation of each side of the bell could contribute to improved low speed manoeuvrability over propellers and traditional control surfaces [53], with the ability to provide thrust vectoring by variation in pressurisation rate and magnitude across buckling tubes.

4. Conclusions

Repeated buckling and unbuckling of flexible tubes can generate consistent thrust through pulse jetting in water. A 60 kPa pressure range inside flexible tubes coupled to a constant stiffness spring was sufficient to produce large amplitudes of $\sim 29^{\circ}$, that remained consistent within an actuation frequency range of 0.2-1.1 Hz. This matches the amplitudes and frequencies seen by natural swimmers, and suggests that buckling tubes are suitable for bioinspired propulsors. The mechanism was used to propel a soft jellyfish-inspired robot through water, where increased pulse frequency led to a predictable increase in velocity, with instantaneous velocities of up to 5 cms⁻¹. The analysis shows that future efforts should investigate material and spring choices to further increase the thrust generation at low frequencies, and consider imposing a lag on the buckling via rapid depressurisation and increased paddle drag. Dynamic efficiency measurements should be incorporated, in particular when using rapid changes in pressures, to get a better understanding of the power that can be generated through buckling. Independent actuation of each buckling tube can potentially improve low speed manoeuvrability over propellers and traditional control-surfaces. No sign of fatigue was seen

across the 1000 pressure cycles performed. To better understand the impact of fatigue on cyclic buckling, it is recommended to investigate performance over a larger number of actuation cycles.

Data availability statement

The data cannot be made publicly available upon publication because they are not available in a format that is sufficiently accessible or reusable by other researchers. The data that support the findings of this study are available upon reasonable request from the authors.

Acknowledgments

This work was made possible through the Civil, Maritime and Environmental Engineering (CMEE) internship scheme at the University of Southampton and through the doctoral training award from the School of Engineering at the University of Southampton.

Author contributions

Alexander O'Loughlin © 0009-0007-7721-0187 Conceptualization (equal), Data curation (lead), Formal analysis (lead), Investigation (lead), Methodology (lead), Validation (lead), Visualization (lead), Writing – original draft (lead), Writing – review & editing (equal)

Samuel Simmons © 0009-0004-6761-9454 Methodology (supporting), Resources (supporting), Supervision (supporting)

Melike Kurt © 0000-0001-6711-7025 Conceptualization (equal), Funding acquisition (supporting), Investigation (supporting), Methodology (supporting), Project administration (supporting), Supervision (equal), Writing – review & editing (equal)

Blair Thornton © 0000-0003-4492-622X Conceptualization (lead), Funding acquisition (lead), Investigation (supporting), Methodology (supporting), Project administration (lead), Resources (lead), Supervision (equal), Writing – review & editing (equal)

References

- [1] Williams S B *et al* 2012 Monitoring of benthic reference sites: using an autonomous underwater vehicle *IEEE Robot*. *Autom. Mag.* 19 73–84
- [2] Massot-Campos M, Bonin-Font F, Guerrero-Font E, Martorell-Torres A, Abadal M M and Muntaner-Gonzalez C 2023 Assessing benthic marine habitats colonized with posidonia oceanica using autonomous marine robots and deep learning: a eurofleets campaign *Estuar. Coastal Shelf Sci.* 291 108438

- [3] McDonald M A, Hildebrand J A and Wiggins S M 2006 Increases in deep ocean ambient noise in the Northeast Pacific west of San Nicolas Island, California J. Acoust. Soc. Am. 120 711–8
- [4] Hildebrand J A 2009 Anthropogenic and natural sources of ambient noise in the ocean Mar. Ecol. Progr. Ser. 395 5–20
- [5] Sezen S and Atlar M 2023 Marine propeller underwater radiated noise prediction with the FWH acoustic analogy part 1: assessment of model scale propeller hydroacoustic performance under uniform and inclined flow conditions Ocean Eng. 279 114552
- [6] Gemmell B J, Costello J H, Colin S P, Stewart C J, Dabiri J O and Tafti D 2013 Passive energy recapture in jellyfish contributes to propulsive advantage over other metazoans *Proc. Natl Acad. Sci. USA* 110 17904–9
- [7] Sahin M, Mohseni K and Colin S P 2009 The numerical comparison of flow patterns and propulsive performances for the hydromedusae Sarsia tubulosa and Aequorea victoria J. Exp. Biol. 212 2656–67
- [8] Neil T R and Askew G N 2018 Jet-paddling jellies: swimming performance in the Rhizostomeae jellyfish Catostylus mosaicus J. Exp. Biol. 221
- [9] Colin S P, Costello J H, Dabiri J O, Villanueva A, Blottman J B, Gemmell B J and Priya S 2012 Biomimetic and live medusae reveal the mechanistic advantages of a flexible bell margin PLoS One 7 e48909
- [10] Dabiri J O, Colin S P, Costello J H and Gharib M 2005 Flow patterns generated by oblate medusan jellyfish: field measurements and laboratory analyses J. Exp. Biol. 208 1257–65
- [11] Dabiri J O, Colin S P and Costello J H 2007 Morphological diversity of medusan lineages constrained by animal-fluid interactions J. Exp. Biol. 210 1867–73
- [12] Gambini C, Abou B, Ponton A and Cornelissen A M 2012 Micro- and macrorheology of jellyfish extracellular matrix *Biophys. J.* 102 1–9
- [13] Megill W M, Gosline J M and Blake R W 2005 The modulus of elasticity of fibrillin-containing elastic fibres in the mesoglea of the hydromedusa Polyorchis penicillatus J. Exp. Biol. 208 3819–34
- [14] Villanueva A, Bresser S, Chung S, Tadesse Y and Priya S 2009 Jellyfish inspired underwater unmanned vehicle *Electroactive Polymer Actuators and Devices (EAPAD)* vol 7287 (SPIE) p 72871G
- [15] Villanueva A 2013 Biomimetic autonomous robot inspired by the Cyanea capillata (Cyro)
- [16] Bujard T 2021 A resonant squid-inspired robot unlocks biological propulsive efficiency
- [17] Arienti A, Calisti M, Giorgio-Serchi F and Laschi C 2013 Poseidrone: Design of a Soft-Bodied ROV With Crawling, Swimming and Manipulation Ability (IEEE)
- [18] Aracri S, Giorgio-Serchi F, Suaria G, Sayed M E, Nemitz M P, Mahon S and Stokes A A 2021 Soft robots for ocean exploration and offshore operations: a perspective Soft Robot. 8 625–39
- [19] Eloy C 2012 Optimal Strouhal number for swimming animals J. Fluids Struct. 30 205–18
- [20] Taylor G K, Nudds R L and Thomas A L R 2003 Flying and swimming animals cruise at a Strouhal number tuned for high power efficiency Lett. Nat. 425 707–11
- [21] Costello J H, Colin S P, Gemmell B J, Dabiri J O and Kanso E A 2023 A Fundamental Propulsive Mechanism Employed by Swimmers and Flyers Throughout the Animal Kingdom (Company of Biologists Ltd)
- [22] Micklem L, Weymouth G D and Thornton B 2022 Energy-efficient tunable-stiffness soft robots using second moment of area actuation
- [23] Irshaidat M, Soufian M, Al-Ibadi A and Nefti-Meziana S 2019 A Novel Elbow Pneumatic Muscle Actuator for Exoskeleton Arm in Post-Stroke Rehabilitation 2nd IEEE Int. Conf. on Soft Robotics (RoboSoft) (IEEE) pp 630–5

- [24] Tiwari R, Meller M A, Wajcs K B, Moses C, Reveles I and Garcia E 2012 Hydraulic artificial muscles J. Intell. Mater. Syst. Struct. 23 301–12
- [25] Chou C P, Hannaford B 1996 rement and ding of McKibben pneumatic artificial muscles 1
- [26] Lopez M and Haghshenas-Jaryani M 2023 A study of energy-efficient and optimal locomotion in a pneumatic artificial muscle-driven snake robot *Robotics* 12 89
- [27] Shintake J, Shea H and Floreano D 2016 Biomimetic Underwater Robots Based on Dielectric Elastomer Actuators IEEE/RSJ Int. Conf. on Intelligent Robots and Systems (IROS) (IEEE)
- [28] Feng W, Sun L, Jin Z, Chen L, Liu Y and Xu H 2024 A large-strain and ultrahigh energy density dielectric elastomer for fast moving soft robot *Nat. Commun.* 15 4222
- [29] Brochu P and Pei Q 2010 Advances in dielectric elastomers for actuators and artificial muscles *Macromol. Rapid Commun.* 31 10–36
- [30] Bigue J-P L and Plante J-S 2013 Experimental study of dielectric elastomer actuator energy conversion efficiency IEEE/ASME Trans. Mech. 18 169–77
- [31] Palakodeti R and Kessler M R 2006 Influence of frequency and prestrain on the mechanical efficiency of dielectric electroactive polymer actuators *Mater. Lett.* 60 3437–40
- [32] Wang Y *et al* 2022 Dielectric elastomer actuators for artificial muscles: a comprehensive review of soft robot explorations *KeAi Commun. Co.* 1 308–24
- [33] Weiss E L S and Guzas E L 2024 Effect of long-term sea water exposure via accelerated life testing on dielectric materials
- [34] Mao Z, Kobayashi R, Nabae H and Suzumori K 2024 Multimodal strain sensing system for shape recognition of tensegrity structures by combining traditional regression and deep learning approaches *IEEE Robot. Autom. Lett.* 9 10050-6
- [35] Moored K W and Bart-Smith H 2007 The analysis of tensegrity structures for the design of a morphing wing *Trans. ASME, J. Appl. Mech.* **74** 668–76
- [36] Moored K W, Kemp T H, Houle N E and Bart-Smith H 2011 Analytical predictions, optimization and design of a tensegrity-based artificial pectoral fin *Int. J. Solids Struct*. 48 3142–59
- [37] Kobayashi R, Nabae H, Endo G and Suzumori K 2022 Soft tensegrity robot driven by thin artificial muscles for the exploration of unknown spatial configurations *IEEE Robot.* Autom. Lett. 7 5349–56
- [38] Hsieh P Y and Hou J H 2024 Adaptive stiffness: a biomimetic robotic system with tensegrity-based compliant mechanism (arXiv:2407.05053)
- [39] Ozkan-Aydin Y, Liu B, Carruthers F A, Seide M, Hammond I I I F and Goldman D 2021 Lateral bending and buckling aids biological and robotic earthworm anchoring and locomotion
- [40] Macdonald W 1991 The Biomechanics of Jellyfish Swimming
- [41] MacGillivray P, Anderson E, Wright G and Demon M 1999 Structure and Mechanics of the squid mantle
- [42] Backholm M, Ryu W S and Dalnoki-Veress K 2013 Viscoelastic properties of the nematode Caenorhabditis elegans, a self-similar, shear-thinning worm *Proc. Natl Acad.* Sci. 110 4528–33
- [43] MatWeb, LLC. 1996 Overview of Materials for PVC (Flexible Grade) (available at: www.matweb.com/search/datasheet. aspx?matguid=35691707c40445388b94db19e000c50a)
- [44] MatWeb, LLC. 1996 Overview of materials for Silicone Rubber (available at: www.matweb.com/search/datasheet. aspx?MatGUID=cbe7a469897a47eda563816c86a73520&ckck=1)
- [45] Webber J 1982 Deflections of inflated cylindrical cantilever beams subjected to bending and torsion
- [46] Weymouth G D and Font B 2023 WaterLily,il: a differentiable fluid simulator in Julia with fast heterogeneous execution (arXiv:2304.08159)

- [47] Moored K W and Quinn D B 2017 Inviscid scaling laws of a self-propelled pitching airfoil (arXiv:1703.08225)
- [48] White C 2021 Tunabot Flex: a tuna-inspired robot with body flexibility improves high-performance swimming
- [49] Nishida Y 2013 Hovering type auv tuna-sand and its surveys on smith caldera in izu-ogasawara ocean area OCEANS 1–5
- [50] Kongsberg 2019 Remus 600 autonomous underwater vehicle (available at: www.kongsberg.com/globalassets/maritime/ km-products/product-documents/)
- [51] National Oceanography Centre Boaty McBoatface 2019 (available at: https://noc.ac.uk/education/educational-resources/boaty-mcboatface)
- [52] Yoerger D R et al 2021 A hybrid underwater robot for multidisciplinary investigation of the ocean twilight zone Sci. Robot. 6 eabe1901
- [53] Colin S P, Costello J H, Katija K, Seymour J and Kiefer K 2013 Propulsion in cubomedusae: mechanisms and utility PLoS One 8 e56393